Simulation characteristics of seismic translation and rotation under the nonlinearity in small deformation

Wei Li [1,2], Yun Wang [1,2,*], Chang Chen[1,2], Lixia Sun[1,3]

[1] *"MWMC" group, School of Geophysics and Information Technology, China University of Geosciences, Beijing* 100083*, China*

[2] *State Key Laboratory of Geological Processes and Mineral Resources, China University of Geosciences, Beijing* 100083*, China*

[3] *Sinopec Research Institute of Petroleum Engineering Co., Ltd., Beijing* 102206*, China*

[*] Corresponding author: wangyun@mail.gyig.ac.cn.

Abstract Ground motions consist of three translational motions along orthogonal axes and three rotational motions around the axes. Recording all six seismic components facilitates obtaining comprehensive vector wavefield information and restoring complete ground displacement. Classical elastic dynamics of elastic wave propagation assume linearity in small deformations of medium particles. However, seismic rotational observations reveal significant discrepancies between the directly recorded rotational motions in the near field and those derived from calculations based on the traditional theory. Considering that nonlinear effects might be pivotal in contributing to this discrepancy, this study incorporates the previously neglected nonlinearity in small deformation into elastodynamic principles to derive velocity-stress elastic wave equations and apply the staggered-grid finite-difference method to simulate the

propagation of seismic waves. The staggered-grid finite-difference method is then employed to simulate the propagation of seismic waves. Simulations were conducted for the translational and rotational components induced by isotropic (ISO), double couple (DC), and compensated linear vector dipole (CLVD) sources—the three fundamental seismic source types described by moment tensor. These simulations allowed for a comparison of the influence of nonlinearity on wavefield anomalies. The results indicate that the error associated with linear approximation is more pronounced in ISO and CLVD source simulations. The nonlinear effect exhibits a greater impact on rotational motions than translational components, particularly in strong earthquakes. We simulated two actual seismicities Taiwan and compared the synthetic records under linear and nonlinear models. Further explorations are still needed to investigate the specific influence of complex propagation path properties and seismic source mechanisms on nonlinear effects.

1 Introduction

Seismic rotational motions can be recorded in ground shaking, especially when caused by strong earthquakes (Graizer, 1991; 2010; Zhou et al., 2019). The rotational motions induced by strong earthquakes is particularly prominent in shallow foci and near-field conditions (Kozak, 2009; Sun et al., 2017). In the field of architecture engineering, rotation is encouraged to be considered in assessing the stability of ground motions and building design (Li, 1991; Li and Sun, 2001; Yan, 2017; Huras et al., 2021). Several studies suggest that incorporating seismic rotation data, which captures spatial gradients, can enhance the precision of earthquake source prediction and moment tensor inversion (Bernauer et al., 2014; Donner, 2016; Ichinose et al., 2021), as supported by simulations conducted by Hua and Zhang (2022).

Lee (2007) summarized applications of observing seismic rotations on seismic engineering and inferred that the seismic rotations should mainly contribute to the nonlinear elasticity and site effect, since the real rotational components measured in strong ground motion are greater 1-2 order than the derived ones from translational components. Recognizing the pivotal role of nonlinear waves in addressing geophysical complexities stemming from Earth's heterogeneities, various analytical solutions of nonlinear wave equations have been developed through iterative techniques in Green's function (McCall, 1994). These include the flux-corrected transport method (Yang et al., 2002; Zheng et al., 2006) and perturbation approaches (Bataille and Contreras, 2009; Jia et al., 2020) to investigate the nonlinear effects on elastic waves. However, most studies primarily focus on the nonlinear constitutive

relations between stress and strain, based on small deformation and its linearization assumption (Renaud et al., 2012; 2013; TenCate et al., 2016; Feng et al., 2018). There is a scarcity of exploration into the nonlinearity of deformations, which may represent a crucial aspect for better approximating rotational motions of strong earthquakes and near-field conditions.

Taiwan, situated in an active seismic zone, broadband seismic observations and studies of physical studies of seismic sources have presented that there are non-ignorable rotational motions in Taiwan's earthquakes and showed different strike-slip rotation characteristics in the south and north of the island (Yu et al., 1999; Wang and Lv, 2006). Oliveira and Bolt (1989) estimated rotational components of strong motions and verified that the rotation effect could not be neglected in near-field observations on Taiwan Island. Using measured six-component ground motion data of 52 earthquakes during 2007-2008 at HGSD station in eastern Taiwan, Chen et al. (2014) pointed out the existence of large vertical rotational motions at near-seismic locations and significant differences in energy and spectral characteristics of horizontal and vertical rotational motions. These studies show the importance of seismic rotation in elucidating Taiwan's subsurface structures and geodynamics.

In this research, we derive the nonlinear wave equations and discuss the rotation characteristics under the nonlinearity in small deformation through numerical simulations of three fundamental seismic moment tensor sources. Furthermore, we engage in theoretical simulations of six-component (6C) wavefields of a near and a strong seismicities in Taiwan to discuss the effects of nonlinearity.

2 Theory and method

2.1 Elastodynamic theory

In a three-dimensional orthogonal Cartesian coordinate system, an elastic body within elastic space, as illustrated in Fig. 1, point A within the elastic body is denoted as **x**. Point B is adjacent to the point A, indicated as **x**+d**x**. The infinitesimal distance separating A and B is defined as ds. Upon instantaneous motivation of an external force, the elastic mass element AB undergoes a displacement $\boldsymbol{u}(\boldsymbol{x}, t)$, to a new location A'B'. This displacement is accompanied by small deformation of the elastic body, where the new positions of A' and B' are designated as **x**' and **x**'+d**x**', respectively, with their distance denoted as ds'. The work done by the external force is primarily converted into kinetic energy due to the displacement and potential energy stemming from the elastic deformation. The deformation is quantified by the change in the square of the length of the line element before and after deformation, i.e., the squared difference in distance between AB and A'B', which is mathematically expressed through Eq. (1). The following equations and tensors are written using dummy index notation rules.

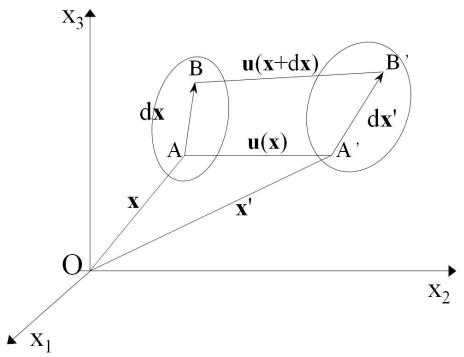

Figure 1. Schematic diagram of displacement and deformation of an elastomer

(Adapted from Aki and Richards (2002))

$$(ds')^2-(ds)^2=\left(\frac{\partial u_j}{\partial x_i}+\frac{\partial u_i}{\partial x_j}+\frac{\partial u_k}{\partial x_i}\cdot\frac{\partial u_k}{\partial x_j}\right)dx_i dx_j,\ i,j\in\{1,2,3\} \tag{1}$$

where u_i and u_j are the displacements along different directions, and x_i and x_j are the Cartesian coordinates. Therefore, Green strain tensor E_{ij}, given by Eq. (2), is an objective measure of deformation before and after applying external force to an elastomer.

$$E_{ij}=\frac{1}{2}\left(\frac{\partial u_j}{\partial x_i}+\frac{\partial u_i}{\partial x_j}+\frac{\partial u_k}{\partial x_i}\cdot\frac{\partial u_k}{\partial x_j}\right),\ i,j\in\{1,2,3\} \tag{2}$$

Within the elastodynamic theory, strain (e_{ij}) and rotation (r_{ij}) tensors are defined as follows:

$$e_{ji}=\frac{1}{2}\left(\frac{\partial u_j}{\partial x_i}+\frac{\partial u_i}{\partial x_j}\right) \tag{3}$$

$$r_{ji}=\frac{1}{2}\left(\frac{\partial u_i}{\partial x_j}-\frac{\partial u_j}{\partial x_i}\right) \tag{4}$$

Based on Eqs. (3) and (4), the Green strain tensor can also be written as Eq. (5).

$$E_{ij}=e_{ij}+\frac{1}{2}e_{ij}^2+\frac{1}{2}\left(e_{ij}r_{ij}-r_{ij}e_{ij}\right)-\frac{1}{2}r_{ij}^2,\ i,j\in\{1,2,3\} \tag{5}$$

The second-order nonlinear displacements in Eq. (2) are neglected in the classical elastodynamic theory, which focuses on the first-order linear terms and neglecting the second-order terms of the strain tensor and the rotation tensor in Eq. (5), thereby reducing the Green strain tensor to its linear approximation e_{ij}.

In isotropic elastic materials, the relationship between strain and stress used to characterize an elastomer is:

$$\sigma_{ij}=\lambda\delta_{ij}e_{kk}+2\mu e_{ij},\ i,j\in\{1,2,3\} \tag{6}$$

where λ and μ are Lamé coefficients, and δ is the Kronecker symbol. Normally, the equation uses the conventional linear approximation e_{ij}, and the principal strains: $\theta=\partial u_1/x_1+\partial u_2/x_2+\partial u_3/x_3=e_{11}+e_{22}+e_{33}$. Include the nonlinearity during elastomer's deformation by using the strain tensor E_{ij} and the principal strains $\theta_E=E_{11}+E_{22}+E_{33}$ in Eq. (6). The Eq. (6) can be simply written as Eq. (7).

$$\sigma_{ij} = \lambda\delta_{ij}E_{kk} + 2\mu E_{ij},\ i,j\in\{1,2,3\} \tag{7}$$

Then, substituting Eq. (7) containing nonlinear contributions into Eq. (8) representing the stress-strain relationship yields Eq. (9), where ρ is the material density.

$$\rho\frac{\partial^2 u_i}{\partial t^2} = \frac{\partial\sigma_{ji}}{\partial x_j},\ i,j\in\{1,2,3\} \tag{8}$$

$$\rho\frac{\partial^2 u_i}{\partial t^2} = \frac{\partial}{\partial x_j}\left(\lambda E_{kk}\delta_{ij} + 2\mu E_{ij}\right) = (\lambda+\mu)\frac{\partial\theta}{\partial x_i} + \mu\frac{\partial^2 u_i}{\partial x_j\partial x_j} + \lambda\delta_{ij}\frac{\partial^2 u_k}{\partial x_i x_j}\cdot\frac{\partial u_k}{\partial x_j} + \mu\left(\frac{\partial^2 u_k}{\partial x_i x_j}\cdot\frac{\partial u_k}{\partial x_j} + \frac{\partial^2 u_k}{\partial x_j x_j}\cdot\frac{\partial u_k}{\partial x_i}\right),$$

$$i,j\in\{1,2,3\} \tag{9}$$

In Eq. (9), the first two terms on the right side of the equal sign are the results of the wave equation under the linear strain tensor, and the last two terms are the increased terms in the wave equation after the nonlinear strain is applied. Eq. (9) shows the difference in equation expression between using the linear and nonlinear strains.

Compared to the original equation which contains only the first two terms of the right of the equal sign in Eq. (9). The nonlinearity introduces several third-order terms that add more physical complexity via material's elastic property. The part associated with the bulk modulus λ reflects that the volumetric deformation is no longer limited to the original purely linear principal strains but also the volumetric change induced by

shear deformation, which is an important feature of the material's nonlinear elastic behavior. The part related to the shear modulus μ additionally describes the shear deformation property. The elastic shear deformation is not merely a direct consequence of shear stress but also exhibits a correlation with the principal strains shown in Eq. (9). The additional terms in Eq. (9) do not directly correspond to the wavefield difference, and in earthquakes, their manifestation may vary depending on the material properties and source loading. Therefore, it is necessary to assess the effect of the material's nonlinear elasticity on seismic wave propagation by specific theoretical numerical simulations.

2.2 Staggered-grid finite-difference simulation method

The staggered-grid finite-difference method has been a technique for numerical simulations of seismic wavefields. In this method, the medium is divided into two grid systems and velocity-stress wave equations are discretized in these grids, thereby allowing computing the numerical solution of wavefields at each grid point as time progresses (Madariaga, 1976; Sun et al., 2018). For example, the grid configuration for a two-dimensional scenario is shown in Fig. 2.

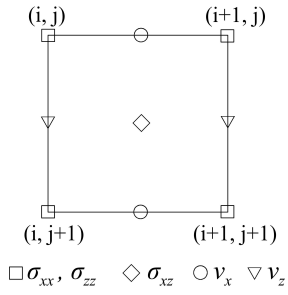

Figure 2. Schematic diagram of 2D staggered grids

Similar to the process of obtaining the velocity-stress equations in three-dimensional (3D) elastic isotropic media using conventional linear strain (Pei,

160 2005). Firstly, the individual stress components using the nonlinear strain **E** are givern

161 in Eq. (10).

$$
\begin{aligned}
\sigma_{xx} &= \lambda\left\{\frac{\partial u_x}{\partial x}+\frac{\partial u_y}{\partial y}+\frac{\partial u_z}{\partial z}+\frac{1}{2}\left[(\frac{\partial u_x}{\partial x})^2+(\frac{\partial u_y}{\partial x})^2+(\frac{\partial u_z}{\partial x})^2+(\frac{\partial u_x}{\partial y})^2+(\frac{\partial u_y}{\partial y})^2+(\frac{\partial u_z}{\partial y})^2+(\frac{\partial u_x}{\partial z})^2+(\frac{\partial u_y}{\partial z})^2+(\frac{\partial u_z}{\partial z})^2\right]\right\}+\mu\left[\frac{\partial u_x}{\partial x}+(\frac{\partial u_x}{\partial x})^2+(\frac{\partial u_y}{\partial x})^2+(\frac{\partial u_z}{\partial x})^2\right]\\
\sigma_{yy} &= \lambda\left\{\frac{\partial u_x}{\partial x}+\frac{\partial u_y}{\partial y}+\frac{\partial u_z}{\partial z}+\frac{1}{2}\left[(\frac{\partial u_x}{\partial x})^2+(\frac{\partial u_y}{\partial x})^2+(\frac{\partial u_z}{\partial x})^2+(\frac{\partial u_x}{\partial y})^2+(\frac{\partial u_y}{\partial y})^2+(\frac{\partial u_z}{\partial y})^2+(\frac{\partial u_x}{\partial z})^2+(\frac{\partial u_y}{\partial z})^2+(\frac{\partial u_z}{\partial z})^2\right]\right\}+\mu\left[\frac{\partial u_y}{\partial y}+(\frac{\partial u_x}{\partial y})^2+(\frac{\partial u_y}{\partial y})^2+(\frac{\partial u_z}{\partial y})^2\right]\\
\sigma_{zz} &= \lambda\left\{\frac{\partial u_x}{\partial x}+\frac{\partial u_y}{\partial y}+\frac{\partial u_z}{\partial z}+\frac{1}{2}\left[(\frac{\partial u_x}{\partial x})^2+(\frac{\partial u_y}{\partial x})^2+(\frac{\partial u_z}{\partial x})^2+(\frac{\partial u_x}{\partial y})^2+(\frac{\partial u_y}{\partial y})^2+(\frac{\partial u_z}{\partial y})^2+(\frac{\partial u_x}{\partial z})^2+(\frac{\partial u_y}{\partial z})^2+(\frac{\partial u_z}{\partial z})^2\right]\right\}+\mu\left[\frac{\partial u_z}{\partial z}+(\frac{\partial u_x}{\partial z})^2+(\frac{\partial u_y}{\partial z})^2+(\frac{\partial u_z}{\partial z})^2\right]\\
\sigma_{xy} &= \sigma_{yx} = \mu\left(\frac{\partial u_x}{\partial y}+\frac{\partial u_y}{\partial x}+\frac{\partial u_x}{\partial x}\frac{\partial u_x}{\partial y}+\frac{\partial u_y}{\partial x}\frac{\partial u_y}{\partial y}+\frac{\partial u_z}{\partial x}\frac{\partial u_z}{\partial y}\right)\\
\sigma_{zy} &= \sigma_{yz} = \mu\left(\frac{\partial u_y}{\partial z}+\frac{\partial u_z}{\partial y}+\frac{\partial u_x}{\partial z}\frac{\partial u_x}{\partial y}+\frac{\partial u_y}{\partial z}\frac{\partial u_y}{\partial y}+\frac{\partial u_z}{\partial z}\frac{\partial u_z}{\partial y}\right)\\
\sigma_{xz} &= \sigma_{zx} = \mu\left(\frac{\partial u_x}{\partial z}+\frac{\partial u_z}{\partial x}+\frac{\partial u_x}{\partial x}\frac{\partial u_x}{\partial z}+\frac{\partial u_y}{\partial x}\frac{\partial u_y}{\partial z}+\frac{\partial u_z}{\partial x}\frac{\partial u_z}{\partial z}\right)
\end{aligned}
\tag{10}
$$

162

163

164 Then, a first-order partial derivative with respect to time is taken on both sides of

165 Eq. (10), with Eq. (8), and the displacement is converted to velocity term, the

166 velocity-stress equations of nonlinear elasticity used for finite-difference method are

167 obtained in Eq. (11):

168

$$
\begin{cases}
\frac{\partial \sigma_{xx}}{\partial x}+\frac{\partial \sigma_{xy}}{\partial y}+\frac{\partial \sigma_{xz}}{\partial z}=\rho\frac{\partial v_x}{\partial t}\\
\frac{\partial \sigma_{yx}}{\partial x}+\frac{\partial \sigma_{yy}}{\partial y}+\frac{\partial \sigma_{yz}}{\partial z}=\rho\frac{\partial v_y}{\partial t}\\
\frac{\partial \sigma_{zx}}{\partial x}+\frac{\partial \sigma_{zy}}{\partial y}+\frac{\partial \sigma_{zz}}{\partial z}=\rho\frac{\partial v_z}{\partial t}
\end{cases}
$$

$$
\begin{cases}
\frac{\partial \sigma_{xx}}{\partial t}=(\lambda+2\mu)\frac{\partial v_x}{\partial x}+\lambda\frac{\partial v_y}{\partial y}+\lambda\frac{\partial v_z}{\partial z}+dt\cdot(\lambda+2\mu)\cdot(\frac{\partial v_x}{\partial x}\frac{\partial v_x}{\partial x}+\frac{\partial v_y}{\partial x}\frac{\partial v_y}{\partial x}+\frac{\partial v_z}{\partial x}\frac{\partial v_z}{\partial x})+dt\cdot\lambda\cdot(\frac{\partial v_x}{\partial y}\frac{\partial v_x}{\partial y}+\frac{\partial v_y}{\partial y}\frac{\partial v_y}{\partial y}+\frac{\partial v_z}{\partial y}\frac{\partial v_z}{\partial y})+dt\cdot\lambda\cdot(\frac{\partial v_x}{\partial z}\frac{\partial v_x}{\partial z}+\frac{\partial v_y}{\partial z}\frac{\partial v_y}{\partial z}+\frac{\partial v_z}{\partial z}\frac{\partial v_z}{\partial z})\\
\frac{\partial \sigma_{yy}}{\partial t}=\lambda\frac{\partial v_x}{\partial x}+(\lambda+2\mu)\frac{\partial v_y}{\partial y}+\lambda\frac{\partial v_z}{\partial z}+dt\cdot\lambda\cdot(\frac{\partial v_x}{\partial x}\frac{\partial v_x}{\partial x}+\frac{\partial v_y}{\partial x}\frac{\partial v_y}{\partial x}+\frac{\partial v_z}{\partial x}\frac{\partial v_z}{\partial x})+dt\cdot(\lambda+2\mu)\cdot(\frac{\partial v_x}{\partial y}\frac{\partial v_x}{\partial y}+\frac{\partial v_y}{\partial y}\frac{\partial v_y}{\partial y}+\frac{\partial v_z}{\partial y}\frac{\partial v_z}{\partial y})+dt\cdot\lambda\cdot(\frac{\partial v_x}{\partial z}\frac{\partial v_x}{\partial z}+\frac{\partial v_y}{\partial z}\frac{\partial v_y}{\partial z}+\frac{\partial v_z}{\partial z}\frac{\partial v_z}{\partial z})\\
\frac{\partial \sigma_{zz}}{\partial t}=\lambda\frac{\partial v_x}{\partial x}+\lambda\frac{\partial v_y}{\partial y}+(\lambda+2\mu)\frac{\partial v_z}{\partial z}+dt\cdot\lambda\cdot(\frac{\partial v_x}{\partial x}\frac{\partial v_x}{\partial x}+\frac{\partial v_y}{\partial x}\frac{\partial v_y}{\partial x}+\frac{\partial v_z}{\partial x}\frac{\partial v_z}{\partial x})+dt\cdot\lambda\cdot(\frac{\partial v_x}{\partial y}\frac{\partial v_x}{\partial y}+\frac{\partial v_y}{\partial y}\frac{\partial v_y}{\partial y}+\frac{\partial v_z}{\partial y}\frac{\partial v_z}{\partial y})+dt\cdot(\lambda+2\mu)\cdot(\frac{\partial v_x}{\partial z}\frac{\partial v_x}{\partial z}+\frac{\partial v_y}{\partial z}\frac{\partial v_y}{\partial z}+\frac{\partial v_z}{\partial z}\frac{\partial v_z}{\partial z})\\
\frac{\partial \sigma_{xy}}{\partial t}=\mu(\frac{\partial v_y}{\partial x}+\frac{\partial v_x}{\partial y})+dt\cdot2\mu\cdot(\frac{\partial v_x}{\partial x}\frac{\partial v_x}{\partial y}+\frac{\partial v_y}{\partial x}\frac{\partial v_y}{\partial y}+\frac{\partial v_z}{\partial x}\frac{\partial v_z}{\partial y})\\
\frac{\partial \sigma_{xz}}{\partial t}=\mu(\frac{\partial v_x}{\partial z}+\frac{\partial v_z}{\partial x})+dt\cdot2\mu\cdot(\frac{\partial v_x}{\partial z}\frac{\partial v_x}{\partial x}+\frac{\partial v_y}{\partial z}\frac{\partial v_y}{\partial x}+\frac{\partial v_z}{\partial z}\frac{\partial v_z}{\partial x})\\
\frac{\partial \sigma_{yz}}{\partial t}=\mu(\frac{\partial v_z}{\partial y}+\frac{\partial v_y}{\partial z})+dt\cdot2\mu\cdot(\frac{\partial v_x}{\partial y}\frac{\partial v_x}{\partial z}+\frac{\partial v_y}{\partial y}\frac{\partial v_y}{\partial z}+\frac{\partial v_z}{\partial y}\frac{\partial v_z}{\partial z})
\end{cases}
$$

169 (11)

170 where v_i ($i\in\{x,y,z\}$) is the velocity component along the Cartesian coordinate, and dt

171 is the time interval. In addition, the rotation rates around the Cartesian Coordinate

172 axes are:

$$\begin{cases} R_x = \frac{1}{2}(\frac{\partial v_z}{\partial y} - \frac{\partial v_y}{\partial z}) \\ R_y = \frac{1}{2}(\frac{\partial v_x}{\partial z} - \frac{\partial v_z}{\partial x}) \\ R_z = \frac{1}{2}(\frac{\partial v_y}{\partial x} - \frac{\partial v_x}{\partial y}) \end{cases} \tag{12}$$

Based on the linear and nonlinear velocity-stress equations Eqs. (11) and (12), We wrote C/C++ language code to numerically simulate the propagation of seismic waves. To weaken boundary reflections, perfectly matched absorbing layer boundary conditions are adapted to the boundaries (Dong and Ma 2000). And acoustic boundary replacement method (shown in Eq. (13)) is employed to ensure the application of free-surface at upper boundary, which defines the free-surface condition at corresponding z-axis position (Xu et al., 2007; Wang et al., 2012)

$$\begin{cases} \sigma_{zz} = 0 \\ \rho = 0.5\rho_0 \\ \lambda = 0 \\ 2\mu = \mu_0 \end{cases} \tag{13}$$

where σ_{zz}, ρ, λ, and μ represent the normal stress, medium density, and Lamé coefficients at and above the free surface, respectively. ρ_0 and μ_0 represent the medium density and Lamé coefficients below the free surface, respectively.

3 Simulations of basic seismic moment sources

3.1 Forward modelling parameters

In the physical process of seismic sources, when the seismic wavelength of interest exceeds the scale of involved source, the source can be regarded as a point source. The seismic moment tensor, as represented in Eq. (14), is the most comprehensive depiction of the seismic point source (Gilbert, 1971).

$$\boldsymbol{M} = \begin{pmatrix} M_{xx} & M_{xy} & M_{xz} \\ M_{yx} & M_{yy} & M_{yz} \\ M_{zx} & M_{zy} & M_{zz} \end{pmatrix} \tag{14}$$

The moment tensor **M** is a symmetric second-order matrix, with each element representing a moment component acting in corresponding direction. It describes the distribution of stress at epicenter and is a crucial parameter for understanding the properties of seismic radiation fields. The moment tensor can be decomposed into three distinct components: isotropy component (ISO), double couple component (DC), and compensated linear vector dipole component (CLVD) (Knopoff and Randall, 1970; Jost and Hermann, 1989). Specifically, the ISO component represents the volume change of focal area, and its moment tensor is characterized by a non-zero trace and uniform force in three principal axes. The DC component signifies the dislocation of two walls of earthquake-induced fault without any volume variation. The moment tensor of the CLVD component consists of three vector dipoles as ISO, characterized by one dipole being twice as large as the other two. The expressions for these three basic seismic source components can be written as shown below. Understanding the wavefield characteristics of these three representative basic seismic sources is important to understanding seismic radiation and the propagation of seismic waves.

$$\boldsymbol{M}^{ISO} = \begin{pmatrix} M_{xx} & 0 & 0 \\ 0 & M_{yy} & 0 \\ 0 & 0 & M_{zz} \end{pmatrix} \tag{15}$$

$$\boldsymbol{M}^{DC} = \begin{pmatrix} 0 & M_{xy} & 0 \\ M_{yx} & 0 & 0 \\ 0 & 0 & 0 \end{pmatrix} \tag{16}$$

$$\boldsymbol{M}^{CLVD}=\begin{pmatrix} M_{xx} & 0 & 0 \\ 0 & M_{yy} & 0 \\ 0 & 0 & -2M_{zz} \end{pmatrix} \tag{17}$$

According to the implementation of seismic moment sources in finite-difference method Graves (1996), the body force represented by the moment tensor can be converted into a velocity source by adding it to velocity components. The specific loading equations for the three moment sources in the grid system are Eqs. (18), (19), and (20).

$$\text{ISO}: \begin{cases} \Delta v_x^{n+\frac{1}{2}}\left(i+\frac{1}{2},j,k\right)=\frac{M_{xx}dt}{\rho Vdx}f^n \\ \Delta v_x^{n+\frac{1}{2}}\left(i-\frac{1}{2},j,k\right)=\frac{-M_{xx}dt}{\rho Vdx}f^n \\ \Delta v_y^{n+\frac{1}{2}}\left(i,j+\frac{1}{2},k\right)=\frac{M_{yy}dt}{\rho Vdy}f^n \\ \Delta v_y^{n+\frac{1}{2}}\left(i,j-\frac{1}{2},k\right)=\frac{-M_{yy}dt}{\rho Vdy}f^n \\ \Delta v_z^{n+\frac{1}{2}}\left(i,j,k+\frac{1}{2}\right)=\frac{M_{zz}dt}{\rho Vdz}f^n \\ \Delta v_z^{n+\frac{1}{2}}\left(i,j,k-\frac{1}{2}\right)=\frac{-M_{zz}dt}{\rho Vdz}f^n \end{cases} \tag{18}$$

$$\text{DC}: \begin{cases} \Delta v_x^{n+\frac{1}{2}}\left(i+\frac{1}{2},j,k\right)=\frac{-M_{xy}dt}{\rho Vdy}f^n \\ \Delta v_x^{n+\frac{1}{2}}\left(i+\frac{1}{2},j-1,k\right)=\frac{M_{xy}dt}{\rho Vdy}f^n \\ \Delta v_y^{n+\frac{1}{2}}\left(i,j-\frac{1}{2},k\right)=\frac{M_{yx}dt}{\rho Vdx}f^n \\ \Delta v_y^{n+\frac{1}{2}}\left(i+1,j-\frac{1}{2},k\right)=\frac{-M_{yx}dt}{\rho Vdx}f^n \end{cases} \tag{19}$$

$$\text{CLVD}: \begin{cases} \Delta v_x^{n+\frac{1}{2}}\left(i+\frac{1}{2},j,k\right)=\frac{M_{xx}dt}{\rho Vdx}f^n \\ \Delta v_x^{n+\frac{1}{2}}\left(i-\frac{1}{2},j,k\right)=\frac{-M_{xx}dt}{\rho Vdx}f^n \\ \Delta v_y^{n+\frac{1}{2}}\left(i,j+\frac{1}{2},k\right)=\frac{M_{yy}dt}{\rho Vdy}f^n \\ \Delta v_y^{n+\frac{1}{2}}\left(i,j-\frac{1}{2},k\right)=\frac{-M_{yy}dt}{\rho Vdy}f^n \\ \Delta v_z^{n+\frac{1}{2}}\left(i,j,k+\frac{1}{2}\right)=\frac{-2M_{zz}dt}{\rho Vdz}f^n \\ \Delta v_z^{n+\frac{1}{2}}\left(i,j,k-\frac{1}{2}\right)=\frac{2M_{zz}dt}{\rho Vdz}f^n \end{cases} \tag{20}$$

where Δv is the velocity increment, n and dt are the time node and interval, and ρ and V are the medium density and the unit volume of the model. The source-time function f^n corresponds to the amplitude of wavelet at the ndt moment.

In the numerical simulations, the Ricker wavelet with a dominant frequency of 0.5 Hz was utilized as the source wavelet. In order to focus on the influence of nonlinearity on seismic waves generated by different types of moment sources, we currently only discuss the simulations in a 3D homogeneous isotropic full-space model. The model size is 80 km (x) × 80 km (y)× 80 km (z), with 0.5-km grid division in three directions. The medium physical properties are v_p=4400 m/s, v_s=3000 m/s, ρ=2600 kg/m^3. The epicenter is located at the center of the model (40km, 40 km, 40 km). The time sampling interval is 15 ms, and the total recording time spans 9 seconds, using second-order time and sixth-order spatial difference approximation.

3.2 Results

3.2.1 ISO source

Under the wave equations containing nonlinearity in small deformation, Fig. 3a displays 8th second 6C wavefield snapshots induced by the ISO source, revealing consistent P-wave amplitudes in translational components but near absence in rotational components.

Fig. 3b highlights wavefield differences between linear and nonlinear conditions, showing that P waves persist in translational components but are very weak in rotation, where S-waves unexpectedly emerge. ISO sources generate P waves, and in linear theory, since the volume change of elastic material is solely associated with a pure pressure field of compression or expansion. So, only P-waves propagate in homogeneous and isotropic media. However, Fig. 3b demonstrates unique nonlinear

media characteristics, enabling P-S wave coupling and energy conversion. This occurs due to nonlinear volumetric strain terms related to shear strains, disrupting linear theory's independent P-S wave propagation constraint.

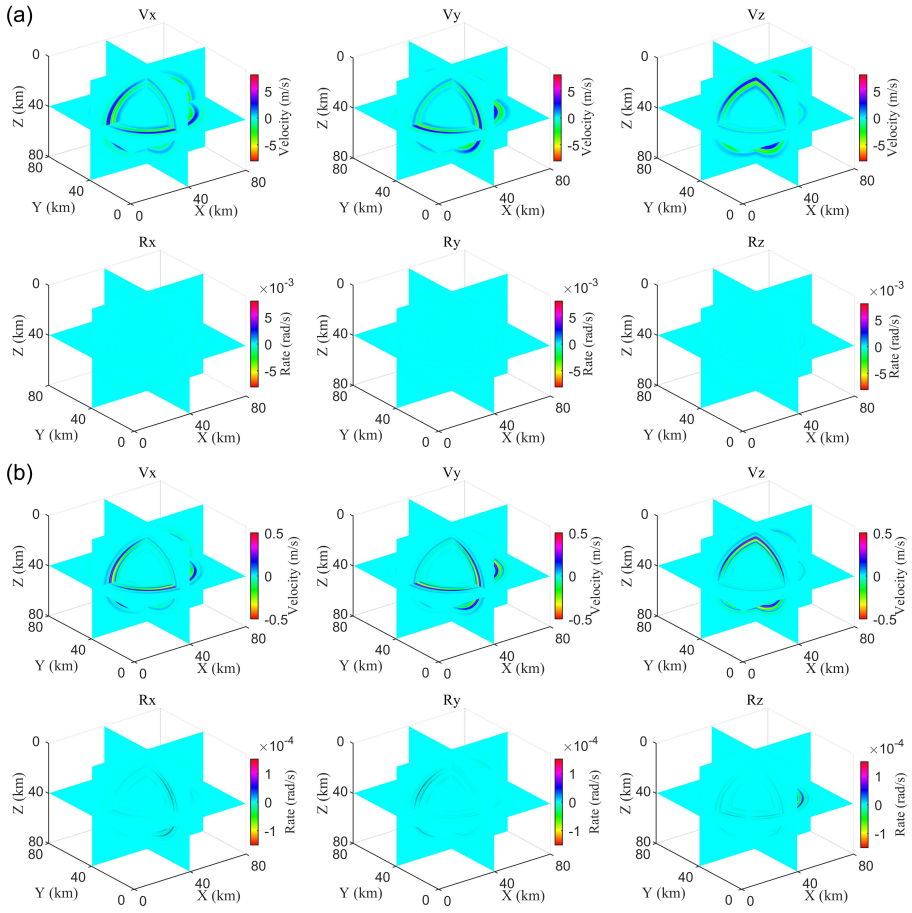

Figure 3. Snapshots of (a) 6C wavefield in nonlinear model and (b) wavefield difference between linear and nonlinear models at 8th second excited by ISO source (Mw7)

3.2.2 DC source

The wavefields excited by the DC source in the nonlinear model are illustrated in Fig. 4a. The DC source primarily generates S-waves with higher energy, with P-waves being comparatively weaker. The loaded force couple, Mxy and Myx, enhances the

waves in the Vx and Vy components relative to the Vz component. Similarly, the Rz-component waves are more pronounced than in the Rx and Ry components. Wavefield difference in Fig. 4b shows nearly one order of magnitude difference in intensity between the difference wavefields and the original wavefields. P- and S-wave intensities are nearly equal in translational components, while S-waves dominate in Rx and Ry components.

In addition, Fig. 4b reveals distinct wavefront polarities for P and S waves influenced by nonlinear terms, differing from those in Fig. 4a. This indicates that nonlinear effects on seismic waves from DC-type source may differ from those of ISO-type source. That is, nonlinearity's impact on seismic waves from shear force sources contrasts with pressure sources, potentially being more complex and leading to the deviations of polarity of wavefield from the original wavefield.

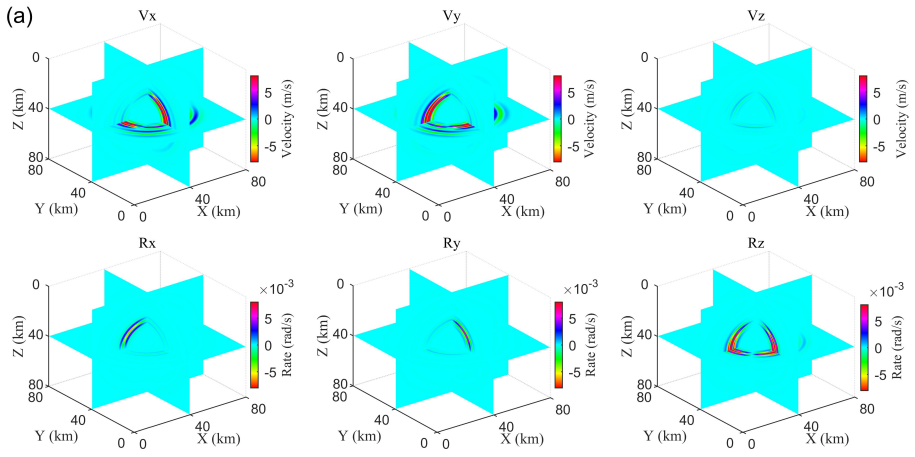

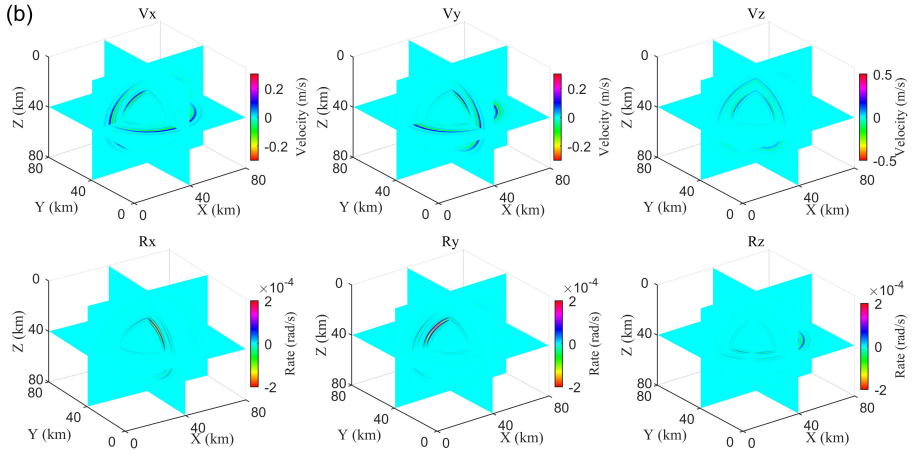

Figure 4. Snapshots of (a) 6C wavefield in nonlinear model and (b) wavefield difference between linear and nonlinear models at 8th second excited by DC source (Mw7)

3.2.3 CLVD source

Fig. 5a displays the results for the CLVD source simulation. The intensities of P- and S-waves are approximately equal in the translational components, whereas in the rotational components, S-waves dominate with the Rz component being notably weaker. The wavefield discrepancies shown in Fig. 5b emphasize the significant intensity of S-wave discrepancies in the rotational components, underscoring their superiority in capturing S-waves propagating through nonlinear media.

It is evident that the polarity of wavefield discrepancies due to nonlinearity in the CLVD source simulation aligns with that observed in the DC source simulation (Fig. 4b). The results may suggest that since both CLVD and DC-type force sources generate seismic waves in a non-volumetric manner, nonlinearity leads to particularly prominent volume changes due to shear stresses. This similarity may arise from their shared force characteristics of the seismic sources, resulting in comparable nonlinear

response characteristics.

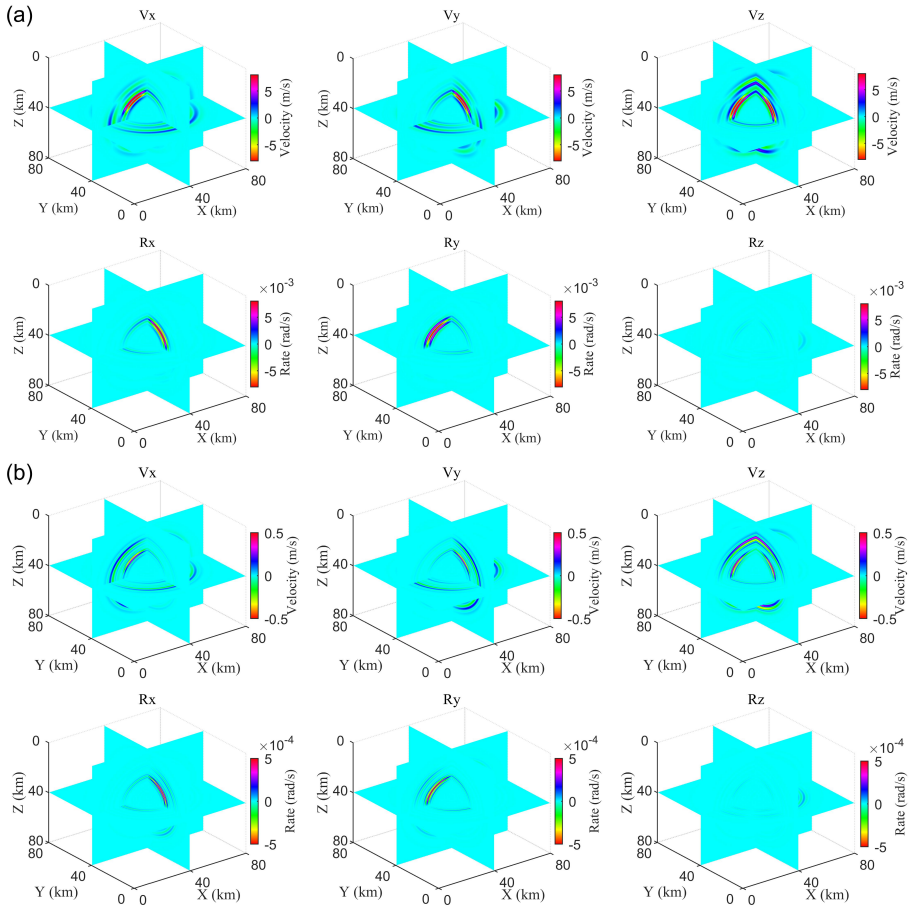

Figure 5. Snapshots of (a) 6C wavefield in nonlinear model and (b) wavefield difference between linear and nonlinear models at 8th second excited by CLVD source (Mw7)

3.3 Wavefield comparisons

The comparison highlights disparities in wavefields of nonlinear elastic waves across both translational and rotational components. We synthesized the seismic wavefield for moment magnitudes ranging from 2 to 7 and analyzed wavefield energy E variations at 6th second of propagation for the three source simulations in both nonlinear and linear models (Fig. 6). The wavefield energy was approximated using Eq. (21):

298 $$E = \sum_{i,j,k} v_{i,j,k}^2 \Delta V \quad (21)$$

299 where $v_{i,j,k}$ is the wavefield value at each grid, and ΔV is the unit grid volume.

300 Fig. 6 displays variations in nonlinear effects across moment magnitudes. The ISO
301 source (Fig. 6a) exhibits a more significant relative error in the wavefield compared to
302 the CLVD source (Fig. 6b), while the DC source (Fig. 6c) yields the most minor
303 relative error among the three models. Across these sources, the wavefield energy
304 change rate increases exponentially with magnitude. At magnitude 7, the rate reaches
305 10% for the ISO source and 5% for the CLVD source. For magnitudes below 4,
306 nonlinear effects are minimal. However, in moderate-to-large earthquakes
307 (magnitudes > 4), the relative alteration in the rotational components becomes more
308 substantial than in the translational components. Given that the DC source typically
309 dominates focal mechanisms for most earthquakes (Zhao and Zhang, 2022), we infer
310 that the linear approximation suffices for modeling most earthquakes (solely
311 involving body waves). However, this approximation may break down in intense
312 seismic activity, particularly when considering rotational components.

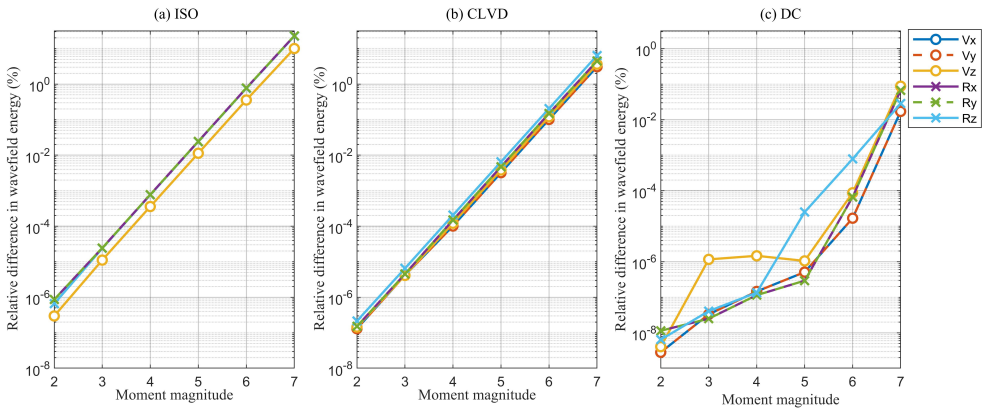

313

314 **Figure 6.** Relative changes in wavefield energy induced by nonlinearity in the

simulations of (a) ISO, (b) CLVD, and (c) DC sources at 6th second with increasing moment magnitude

Fig. 7 showcases the temporal evolution of wavefield energy between nonlinear and linear models for a magnitude 6 earthquake. Within the first 4 to 6 seconds of seismic wave propagation, intricate phase interactions may result in an overall energy reduction. Subsequently, wavefield energy difference due to nonlinearity stabilizes, with a more significant energy increase in the rotational component than the translational components. The ISO source model exhibits the most prominent increase in nonlinear relative error with wave propagation, followed by CLVD-type source (Fig. 7b). In the DC source model, nonlinear effects are minimal, with negligible changes induced by nonlinearity in all components except the Rz component (Fig. 7c).

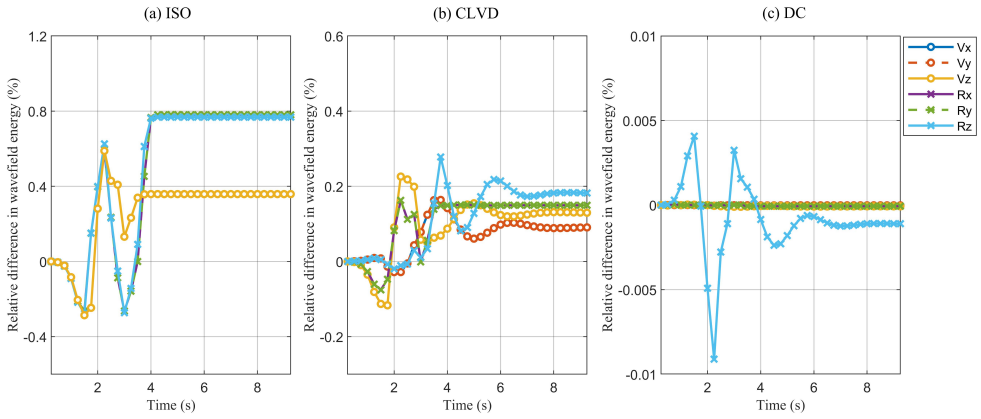

Figure 7. Relative changes in wavefield energy induced by nonlinearity in the simulations of (a) ISO, (b) CLVD, and (c) DC sources (Mw6) with increasing time

Based on the preceding results, current seismometers possess sufficient accuracy to capture nonlinearity-induced anomalies in wavefield intensity as demonstrated in

simulations. However, it is crucial to observe that these simulations exhibiting prominent anomalies utilize larger magnitude seismic sources and model wave propagation over approximately 30 km, representing near-field results. Under such circumstances, the manifestation of nonlinear effects is anticipated to be significant.

In contrast, capturing the nonlinearity on seismic waves in small magnitudes or distant seismicity poses greater challenges. The attenuation and scattering of seismic waves with distance and the relatively lower energy released by smaller magnitudes. Consequently, nonlinear effects may be substantially weakened, heightening the complexity of observation and identification. Thus, given current technological and observational constraints, studying the nonlinear effects of strong earthquakes emerges as a more practical and feasible option.

4 Observations and simulations of two earthquakes

Two earthquakes along the Taiwan coast are referenced to establish seismic models for simulating wave propagation in both linear and nonlinear media. These simulations aim to preliminarily assess the nonlinear effects of more complex seismic source mechanisms. The spatial difference accuracy in these simulations is set to 10th order.

4.1 Hualien earthquakes

Taiwan, situated at the juncture of three prominent tectonic plates—the Philippine Sea Plate, the Eurasia Plate, and the Pacific Ocean Plate—experiences frequent moderate to large earthquakes annually (Zheng et al., 2005). The 2018 Hualien

earthquake (M_W 5.41, referred to as E1) and the 2019 Hualien earthquake(M_W 6.13, referred to as E2) occurred along Taiwan's eastern coastline, with 15-km and 30-km epicenter depths, respectively. The epicenter locations and station configurations, as depicted by GMT (Wessel et al., 2019), are shown in Fig. 8. To directly observe seismic rotational rates, BlueSeis-3A fiber-optic rotational seismometers, characterized by a self-noise of up to $2 \times 10^{-8}\ rad/s/\sqrt{Hz}$ and a bandwidth of 0.001-100 Hz (Bernauer et al., 2018; Cao et al., 2021) were deployed at the Nanao station (NA01) to record E1 and at the Qingyuanshan station (QS01) to record E2.

According to the information from the U.S. Geological Survey (USGS, https://www.usgs.gov/), both E1 and E2 were triggered by reverse faulting mechanisms. The focal mechanisms represented by beach balls are shown in Fig. 8b. The moment tensor parameters of E1 and E2 are detailed in Eqs. (22) and (23), respectively.

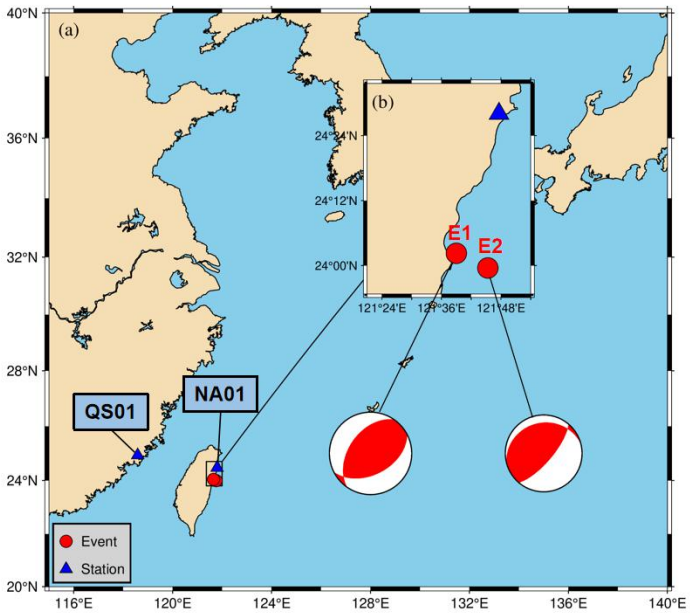

Figure 8. Epicenters and observation sites of E1 and E2

369
$$M_{xx} = -7.569\times10^{16}, M_{yy} = -2.373\times10^{16}, M_{zz} = 9.942\times10^{16}$$
$$M_{xz} = 7.372\times10^{16}, M_{yz} = -1.0965\times10^{17}, M_{xy} = 4.156\times10^{16} \quad (22)$$

370
$$M_{xx} = -1.064\times10^{18}, M_{yy} = -7.607\times10^{17}, M_{zz} = 1.8247\times10^{18}$$
$$M_{xz} = 3.141\times10^{17}, M_{yz} = 3.155\times10^{17}, M_{xy} = 1.114\times10^{18} \quad (23)$$

371

372 4.2 Earthquake simulations

373 To simulate E1 and E2, we implemented free-surface condition at the upper
374 surface and absorbing boundary conditions in other directions of the 3D model.
375 According to the CRUST1.0 model (Laske et al., 2013), the subsurface medium
376 beneath the observation station of E1 is divided into five distinct layers, as detailed in
377 Table 1. Given the region's relatively stable geological structure and the focus of the
378 current study is not exploring how medium properties affect the propagation of
379 nonlinear seismic waves, we adopted a simplified strategy by using same stratigraphic
380 parameter settings for simulating the two earthquakes.

381 **Table 1** Physical properties of media for simulations of E1 and E2

Layer	Thickness (km)	Vp (km/s)	Vs (km/s)	ρ (kg/m³)
1	0.50	2.50	1.07	2.11
2	10.12	5.80	3.40	2.63
3	9.81	6.30	3.62	2.74
4	9.82	6.90	3.94	2.92
5	-	7.70	4.29	3.17

382 **Table 2** Simulation parameters for E1

Items	Parameters
Source type	Eq. (20)
Central frequency	1 Hz
Grid interval	1 km
Time interval	5 ms
Source location	(0, 0, 15 km)
Receiver location	(53 km, 4 km, 0 km)
Recording time	30 s

To simulating E1, the model size is 60 km (x) × 20 km (y) × 30 km (z) to suit the observation syste. The simulation parameters are shown in Table 2.

.Fig. 9a displays the synthetic records of E1, showcasing the direct P- and S-waves, alongside elliptical polarization within the X-Z vertical plane and rotational movements around the Y-axis induced by Rayleigh waves. The large amplitude difference in magnitude between the simulations and the observations can be attributed to the difference between the elastic simulation media and actual viscoelastic media, leading to significant energy attenuation in observations.

Fig. 9b shows the complexity of seismic waves after P- and S-wave arrivals in translational components and R_Z components, influenced by site effect and the nearly northeast strike of the seismogenic fault result in pronounced. This indicates the presence of Love waves and deviations fom the simplified Crust model. The simulated rotational components are significantly weaker (1000 times) than the simulated translational components, yet the observed rotation are only 250 times weaker than the translational ones. This discrepancy may suggest that observed rotation is stronger than the theoretically anticipated. However, multiple factors can affect observed records, and the observed typically exhibit richer high-frequency signals showing stronger rotational energy. So further in-depth analysis and comparison are required before comprehensively identifying and determining the influencing factors.

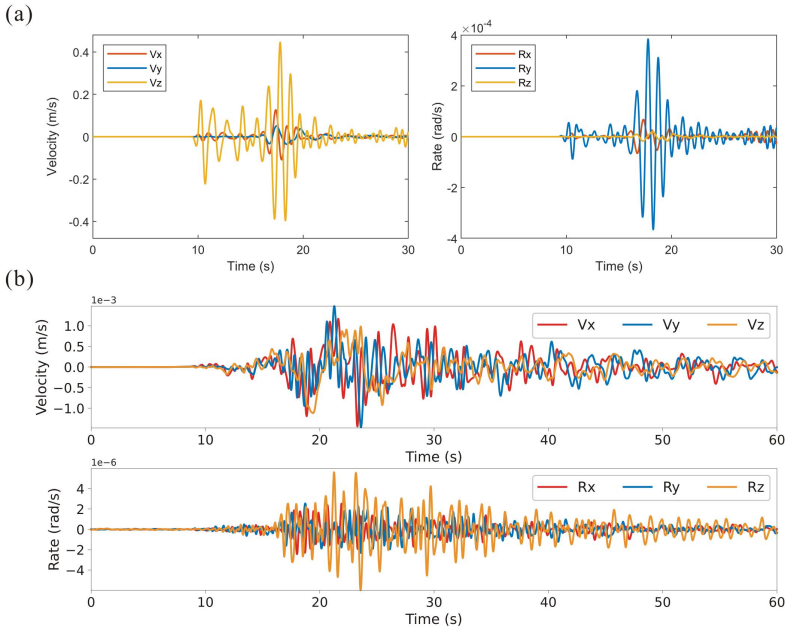

404

405 **Figure 9.** 6C seismic records of (a) simulation under linear small deformation and (b)

406 actual observation for E1. In (b), a band-pass filter of 0.1 Hz to 2 Hz is applied

407

408 Fig. 10 presents a comparision of 6C root-mean-square (RMS) amplitude (Fig.

409 10a) and normalized time-frequency spectrum difference (Fig. 10b) between linear

410 and nonlinear seismic models. RMS amplitudes within a 2-second window were

411 computed at 1-second intervals, with relative change rates derived.

412 Fig. 10a reveals minor RMS amplitude anomalies attributed to nonlinearity, with

413 the rotational components smaller than the translational components, and translational

414 errors not exceeding 0.1%. For the E1 simulation, linear approximation errors are

415 negligible. In Fig. 10b, the seismic phases affected vary in translational and rotational

416 components. Rotational components exhibit greater impact of nonlinearity on direct

417 S-waves and surface waves, whereas in the translational components, particularly in

418 Vx and Vz, nonlinearity shows heightened effects on p-waves, with the surface waves

in the Vy component also affected.

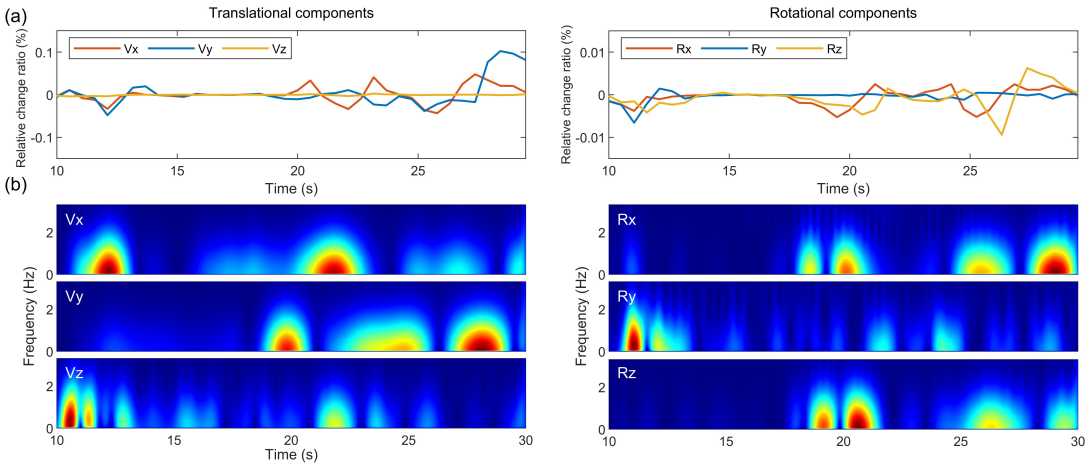

Figure 10. Relative change in RMS amplitude (a) and normalized time-frequency difference (b) of translational components (left subfigures) and rotational components (right subfigures) between linear and nonlinear scenarios

Table 3 Simulation parameters for E2.

Items	Parameters
Source type	Eq. (21)
Central frequency	0.5 Hz
Grid interval	5 km
Time interval	2 ms
Source location	(0, 310 km, 30 km)
Receiver location	(100, 0 km, 0 km)
Recording time	200 s

For simulating E2, the model is 150 km (x) ×350 km (y) × 50 km (z), and the modeling parameters are detailed in Table 3. The synthetic 6C seismic records (Fig. 11a) show a dominance of the Vz component over the Vx and Vy components, while the Rx and Ry components exhibit greater strength than the Rz component, indicating the rotational motions primarily occurring in the horizontal direction. In the actual

observed records (Fig. 11b), where the seismometer is positioned on a solid rock within a tunnel, indicate a slight dominance of the Vz component over the Vx and Vy components, while the Rz component is slightly weaker than the Rx and Ry components, which in general aligns with the relative amplitude strength of theoretical simulations. These observations suggest that the rotational motions for E2 are predominantly horizontal, and the site effect is relatively weaker. The amplitude difference between the actual observed rotational and translational components is smaller than the amplitude difference between the simulated translational and rotational components, consistent with the characteristic shown in Fig. 9.

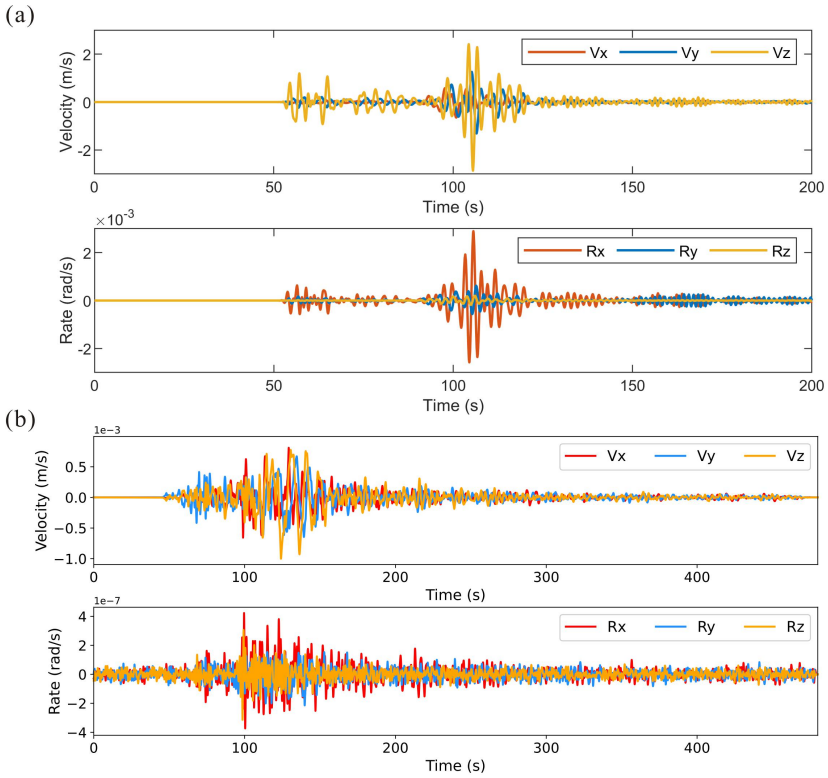

Figure 11. 6C seismic records of (a) simulation under linear small deformation and (b) actual observation for E2. In (b), a band-pass filter of 0.1 Hz to 1 Hz is applied

Fig. 12(a) presents the root mean square (RMS) amplitudes of E2 from linear

simulations, with the results incorporating nonlinearity depicted as error bars. It shows that nonlinearity's impact is more significant on the translational components than the rotational motions (generally longer error bars). The Vz component experiences a greater influence (generally wider error bars) among the translational components, and the the Rx-component RMS amplitude is more affected. Fig. 12(b) illustrates that both direct S-waves and surface waves in both translational and rotational components are primarily affected by nonlinearity, albeit with distinct seismic phases affected within their respective frequency spectra. Additionally, the reflected waves on the Vz component also exhibit considerable errors.

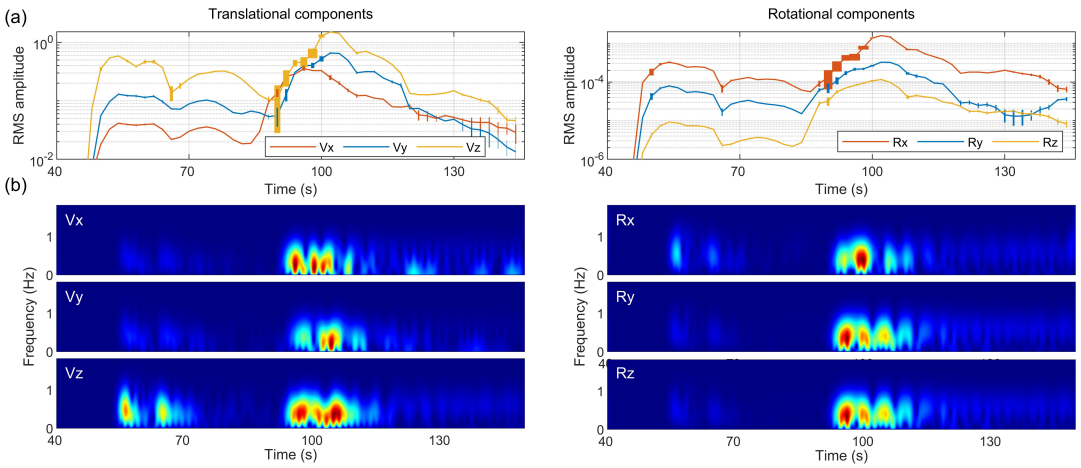

Figure 12. Relative change in RMS amplitude (a) and normalized time-frequency difference (b) of translational components (left subfigures) and rotational components (right subfigures) between linear and nonlinear scenarios

The simulation results in Section 3 indicate that seismic rotational components are affected more than translational components due to nonlinearity. However, these comparisons encompass the entire modeled wavefield. Source radiation

characteristics may introduce angle-dependent nonlinear effects, potentially impacting translational components more than rotation. This underscores the complexity of nonlinearity and emphasizes the ongoing need for in-depth exploration and research in this area.

5 Discussion

In contrast to traditional wave propagation limited to linear terms, the Green strain tensor is expressed as a function encompassing both the strain tensor and the rotation tensor. By incorporating nonlinear components , the elastic wave equations now incorporate third-order derivatives of the displacement field. These higher-order nonlinear terms significantly influence the dynamic properties of seismic waves, affecting both volume changes and shear deformation during material deformation.

While ISO source simulation in nonlinear media suggests potential coupling between P-waves and S-waves, actual observations reveal more intricate nonlinear effects constrained by multiple factors. Although numerical simulations demonstrate S-wave generation, this finding cannot be generalized to all real-world earthquakes. The existence and intensity of S-waves in natural scenarios necessitate further field observation and theoretical research.

Current simulation efforts are preliminary, limited to basic theoretical exploration in idealized homogeneous isotropic elastic media. These models solely focus on three basic moment tensor source types and utilize point source loading. However, natural earthquakes exhibit far greater complexity in source and media characteristics, including diverse fault rupture processes, anisotropic medium properties, site effects

and so on. Factors such as seismic source mechanism, propagation path, surface conditions exert complex and unclear influences on nonlinear effects. These factors interact in complex ways, impacting seismic wave propagation.

Since the mechanics of seismic rotation may be related to nonlinear elasticity (Guyer and McCall, 1995; Guyer and Johnson, 1999), asymmetric moment tensor (Teisseyre et al., 2003; Teisseyre, 2010), medium heterogeneity, anisotropy (Pham et al., 2010; Sun et al., 2021), and site effects, by examining the intimate relationship between nonlinear effects and propagation path and medium characteristics, we can gain a more objective and accurate understanding of the impact of nonlinearity on seismic waves, particularly regarding rotational components.

6 Conclusions

Utilizing seismic wave equations that assume linear small deformations as a foundational framework, we have derived elastic-wave formulations incorporating Green strain tensor's nonlinear components. Through numerical simulations and analyses in models of three fundamental seismic moment sources and two Taiwan earthquakes, to study the wavefield disparities between linear and nonlinear scenarios of both translational and rotational motions. The principal findings of our study can be summarized as follows.

(i) When simulating ISO sources in media with nonlinear effects, the interaction between seismic waves leads to the generation of S-waves. For CLVD and DC sources, nonlinear effects cause the intensities of P-waves and S-waves on translational components to trend towards equilibrium, while S-waves exhibit

prominence on rotational components.

(ii) The impact of nonlinear media on seismic waves varies depending on the source model. The ISO source model is most significantly affected by nonlinear effects, while the DC source model is relatively less affected. As the source intensity increases, the change in seismic wavefield energy caused by nonlinear media exhibits an exponential growth trend.

(iii) In simulations of pure fundamental seismic sources, the error of linear approximation for rotation is more significant in cases of strong earthquakes, while the nonlinear effects produced by microearthquakes and small earthquakes can be ignored. The S-waves and surface waves recorded by seismic rotational components have certain significance for studying the impact of nonlinearity on the propagation characteristics of seismic waves.

(iiii) Rayleigh waves dominate the simplified simulations of E1 and E2, but the presence of Love waves in actual observations may be related to site effects or complex propagation media. The linear approximation error of E1 simulation is very small, while the error of E2 simulation is larger, due to differences in their magnitude and potentially the radiation azimuth of the seismic source that leads to inhomogeneous nonlinear effects.

Author contributions. WL: conceptualization, methodology, investigation, formal analysis, writing - original draft. YW: conceptualization, writing - original draft and revised draft. CC: in vestigation, formal analysis. LS: methodology.

529

530 **Data and resources.** The seismic records of **E**1 are provided by the Institute of Earth
531 Sciences, Academia Sinica, Taiwan, China. The translational records of **E**2 are
532 acquired from the Fujian Earthquake Agency.

533

534 **Competing interests.** The contact author has declared that neither of the authors has
535 any competing interes.

536

537 **Disclaimer.** Publisher's note: Copernicus Publications remains neutral with regard to
538 jurisdictional claims made in the text, published maps, institutional affiliations, or any
539 other geographical representation in this paper.

540

541 **Financial support.** This research is financially supported by the National Natural
542 Science Foundation of China (No. 42150201、No. 62127815、No. U1839208).

543

544 **References**

545 Aki, K., and P. G. Richards. Quantitative seismology, 2nd ed, California: University
546 Science Books, https://doi.org/10.1029/2003EO210008, 2002.
547 Bataille, K., Contreras, M.: Nonlinear elastic effects on permanent deformation due to
548 large earthquakes, Phys. Earth Planet. Inter., 175(1), 47-52,
549 https://doi.org/10.1016/j.pepi.2008.02.016, 2009.
550 Bernauer, F., Wassermann, J., Guattari, F., Frenois, A., Bigueur, A., Gaillot, A., de

551 Toldi, E., Ponceau, D., Schreiber, U., and Igel, H.: BlueSeis3A: Full
552 characterization of a 3C broadband rotational seismometer, Seismol. Res. Lett.,
553 89(2A), 620–629, https://doi.org/10.1785/0220170143, 2018.
554 Bernauer, M., Fichtner, A., and Igel, H.: Reducing nonuniqueness in finite source
555 inversion using rotational ground motions, J. Geophys. Res.-Solid Earth, 119(6),
556 4860-4875, https://doi.org/10.1002/2014JB011042, 2014.
557 Cao, Y. W., Chen, Y. J., Zhou, T., Yang, C. X., Zhu, L. X., Zhang, D. F., Cao, Y. J.,
558 Zeng, W. Y., He, D., and Li, Z. B.: The development of a new IFOG-based 3C
559 rotational seismometer, Sensors, 21(11), 3899, https://doi.org/10.3390/s21113899,
560 2021.
561 Chen, Q. J., Yin, J. E., and Yang, Y. S.: Time-frequency characteristic analysis of
562 six-degree-freedom ground motion records, Chinese Quarterly of Mechanics, 35,
563 (3), 499-506,
564 https://link.oversea.cnki.net/doi/10.15959/j.cnki.0254-0053.2014.03.033, 2014
565 (in Chinese).
566 Dong, L. G., and Ma, Z. T.: A staggered-grid high-order difference method of
567 one-order elastic wave equation, Chinese J. Geophys., 43(3), 411-419, 2000 (in
568 Chinese).
569 Donner, S., Bernauer, M., and Igel, H.: Inversion for seismic moment tensors
570 combining translational and rotational ground motions, Geophys. J. Int., 207(1),
571 562-570, https://doi.org/10.1093/gji/ggw298, 2016.

572 Feng, X., Fehler, M., Brown, S., Szabo, T. L., and Burns, D.: Short-period nonlinear
573 viscoelastic memory of rocks revealed by copropagating longitudinal acoustic
574 waves, J. Geophys. Res.-Solid Earth, 123(5), 3993–4006,
575 https://doi.org/10.1029/2017JB015012, 2018.
576 Graizer, V. M.: Strong motion recordings and residual displacements: what are we
577 actually recording in strong motion seismology? Seismol. Res. Lett., 8(4),
578 635-639, https://doi.org/10.1785/gssrl.81.4.635, 2010.
579 Graizer, V. M.: Inertial seismometry methods, Earth Physics, 27(1), 51-61, 1991.
580 Graves, R. W.: Simulating seismic wave propagation in 3D elastic media using
581 staggered-frid finite differences, Bull. Seismol. Soc. Am., 86(4), 1091-1106,
582 1996.
583 Gilbert, F.: Excitation of the normal modes of the Earth by earthquake sources,
584 Geophys. J. R. astr. Soc, 22(2), 223-226,
585 https://doi.org/10.1111/j.1365-246X.1971.tb03593.x, 2010.
586 Guyer, R. A., and McCall, K. P.: Hysteresis, discrete memory, and nonlinear wave
587 propagation in rock: A new paradigm, Phys. Rev. Lett., 74(17), 3491-3495,
588 https://doi.org/10.1103/physrevlett.74.3491, 1995.
589 Guyer, R. A., and Johnson, P. A.: Nonlinear mesoscopic elasticity: evidence for a new
590 class of materials, Physics Today, 52(4), 30-36, https://doi.org/10.1063/1.882648,
591 1999.
592 Hua, S. B., and Zhang, Y.: Numerical experiments of moment tensor inversion with
593 rotational ground motions, Chinese J. Geophys., 65(1), 197-213,

https://doi.org/10.6038/cjg2022P0668, 2022 (in Chinese).

Huras, L., Zembaty, Z., Bonkowski, P. A., and Bobraet, P.: Quantifying local stiffness loss in beams using rotation rate sensors, Mech. Syst. Signal Proc., 151, 107396, https://doi.org/10.1016/j.ymssp.2020.107396, 2021.

Ichinose, G. A., Ford, S. R., and Mellors, R. J.: Regional moment tensor inversion using rotational observations, J. Geophys. Res.-Solid Earth, 126(2), e2020JB020827, https://doi.org/10.1029/2020JB020827, 2021.

Jia, L., Yan, S. G., Zhang, B. X., and Huang, J.: Research on perturbation method for nonlinear elastic waves, J. Acoust. Soc. Am., 148, EL289–EL294, https://doi.org/10.1121/10.0001980, 2020.

Jost, M. L., and Hermann, R. B.: A students guide to and review of moment tensors, Seism. Res. Lett., 60, 37-57, https://doi.org/10.1785/gssrl.60.2.37, 1989.

Knopoff, L., and Randall M. J.: The compensated linear-vector dipole: A possible mechanism for deep earthquakes, J. Geophy. Res., 75(26), 4957–4963, https://doi.org/10.1029/JB075i026p04957, 1970.

Kozak, J. T.: Tutorial on earthquake rotational effects: historical examples, Bull. Seismol. Soc. Am., 99(2B), 998-1010, https://doi.org/10.1785/0120080308, 2009.

Lai, X. L., and Sun, Y.: Three component rotational ground motion obtained from explosive source data, Earth science, 42(4), 645－651, 2017 (in Chinese).

Laske, G., Masters, G., Ma, Z. T., and Pasyanos, M.: Update on CRUST1. 0-A 1-degree global model of Earth's crust, EGU General Assembly 2013, 15,

616 EGU2013-2658, 2013.

617 Lee, C. E. B., Celebi, M., Todorovska, M. I., and Diggles, M. F.: Rotational
618 seismology and engineering applications — Proceedings for the First
619 International Workshop, Menlo Park, California, U.S.A.—September 18 to 19,
620 2007: U.S. Geological Survey Open-File Report 2007-1144, 46 p.
621 http://pubs.usgs.gov/of/2007/1144/, 2007.

622 Li, H. N.: Study on rotational components of ground motion, Journal of Shenyang
623 Architectural and Civil Engineering Institute, 7(1), 88-93, 1991 (in Chinese).

624 Li, H. N., and Sun, L. Y.: Rotational components of earthquake ground motions
625 derived from surface waves, Earthq. Eng. Eng. Vib., 21(1), 15-23,
626 https://link.oversea.cnki.net/doi/10.13197/j.eeev.2001.01.003, 2001 (in Chinese).

627 Madariaga, R.: Dynamics of an expanding circular fault, Bull. Seismol. Soc. Am.,
628 66(3), 639-666, https://doi.org/10.1007/BF02246368, 1976.

629 McCall, K. R.: Theoretical study of nonlinear elastic wave propagation, J. Geophys.
630 Res., 99(B2), 2591-2600, https://doi.org/10.1029/93JB02974, 1994.

631 Oliveira, C. S., and Bolt, B. A.: Rotational components of surface strong ground
632 motion, Earthq. Eng. Struct. D. 18(4), 517–526,
633 https://doi.org/10.1002/eqe.4290180406, 1989.

634 Pei, Z. L.: Numerical simulation of elastic wave equation in 3-D anisotropic media
635 with staggered-grid high-order difference method, Geophysical Prospecting for
636 Petroleum, 44(4), 308-315, https://doi.org/10.3969/j.issn.1000-1441.2005.04.002,
637 2005 (in Chinese).

638 Pham, N. D., Igel, H., Puente, J. D. L., Käser, M., and Schoenberg, M. A.: Rotational
639 motions in homogeneous anisotropic elastic media, Geophysics 75(55), D47-D56,
640 https://doi.org/10.1190/1.3479489, 2010.
641 Renaud, G., Le Bas, P. Y., and Johnson, P. A.: Revealing highly complex elastic
642 nonlinear (anelastic) behavior of Earth materials applying a new probe: Dynamic
643 acoustoelastic testing, J, Geophys. Res.-Solid Earth, 117, B06202, ,
644 https://doi.org/10.1029/2011JB009127, 2012.
645 Renaud, G., Rivière, J., Le Bas, P. Y., and Johnson, P. A.: Hysteretic nonlinear
646 elasticity of Berea sandstone at low-vibrational strain revealed by dynamic
647 acoustoelastic testing, Geophys. Res. Lett., 40(4), 715-719,
648 https://doi.org/10.1002/grl.50150, 2013.
649 Sun, L., Yu, Y., Lin, J. Q., and Liu, J. L.: Study on seismic rotation effect of simply
650 supported skew girder bridge, Earthquake Engineering and Engineering
651 Dynamics, 37(4), 121-128, https://doi.org/10.13197/j.eeev.2017.04.121.sunl.014,
652 2017 (in Chinese).
653 Sun, L. X., Wang, Y., Li, W., and Wei, Y. X.: The characteristics of seismic rotations
654 in VTI medium, Appl. Sci.-Basel, 11(22), 10845,
655 https://doi.org/10.3390/app112210845, 2021.
656 Sun, L. X., Zhang, Z., and Wang, Y.: Six-component elastic-wave simulation and
657 analysis, EGU General Assembly 2018, Geophysical Research Abstracts, 20,
658 EGU2018-14930-1, 2018.
659 Teisseyre, R., Suchcicki, J., Teisseyre, K. P., Wiszniowski J., and Palangio, P.:
660 Seismic rotation waves: Basic elements of the theory and recordings, Annals of

661 Geophysics, 46(4), 671–685, https://doi.org/10.4401/ag-4375, 2003.
662 Teisseyre, R.: Tutorial on new developments in the physics of rotational motions,
663 Translated World Seismology, 99(2A), 1028-1039,
664 https://doi.org/10.1785/0120080089, 2010.
665 TenCate, J. A., Malcolm, A. E., Feng, X., and Fehler, M. C.: The effect of crack
666 orientation on the nonlinear interaction of a P wave with an S wave, Geophys.
667 Res. Lett., 43(12), 6146-6152, https://doi.org/10.1002/2016GL069219, 2016.
668 Wang, L., Luo, Y. H., and Xu, Y. H.: Numerical investigation of Rayleigh-wave
669 propagation on topography surface, J. Appl. Geophys., 86, 88–97,
670 https://doi.org/10.1016/j.jappgeo.2012.08.001, 2012.
671 Wang, X. S., and Lv, J.: The holistic clockwise rotation possibly existed in Taiwan
672 region - in addition on the seismicity feature and earthquake prediction in its
673 adjacent areas, South China Journal of Seismology, 2, 48-54,
674 https://doi.org/10.3969/j.issn.1001-8662.2006.02.008, 2006 (in Chinese).
675 Wessel, P., Luis, J. F., Uieda, L., Scharroo, R., Wobbe, F., Smith, W. H. F., and Tian,
676 D.: The generic mapping tools version 6, Geochemistry, Geophysics,
677 Geosystems, 20, 5556–5564, https://doi.org/10.1029/2019GC008515, 2019.
678 Xu, Y. X., Xia, J. H., and Miller, R. D.: Numerical investigation of implementation of
679 airearth boundary by acoustic-elastic boundary approach, Geophysics, 72 (5),
680 SM147–SM153, https://doi.org/10.1190/1.2753831, 2007.
681 Yan, Y. Y.: Seismic response analysis of high-rise building under different types of
682 multi-dimensional earthquake ground motions (Ph.D. dissertation), Jiangsu

683 University, 2017(in Chinese).

684 Yu, S. B., Kuo, L. C., and Punongbayan, R. S., Emmanuel, G.R.: GPS observation of
685 crustal deformation in Taiwan-Luzon region, Geophys. Res. Lett., 26(7), 923-926,
686 https://doi.org/10.1029/1999GL900148, 1999.

687 Yang, D.H., Liu, E., Zhang, Z.J., and Teng, J.: Finite-difference modelling in
688 two-dimensional anisotropic media using a flux-corrected transport technique,
689 Geophys. J. Int., 148(2), 320–328,
690 https://doi.org/10.1046/j.0956-540x.2001.01575.x, 2002.

691 Zhao, K. C., and Zhang, X. B.: Distinguishing underground nuclear test by matrix
692 decomposition, Acta Scientiarum Naturalium Universitatis Pekinensis, 58(4),
693 609-614, https://link.oversea.cnki.net/doi/10.13209/j.0479-8023.2022.042, 2022
694 (in Chinese).

695 Zheng, H. S., Z. J. Zhang, and Liu, E. R.: Nonlinear seismic wave propagation in
696 anisotropic media using the flux-corrected transport technique, Geophys. J. Int.,
697 165(3), 943-956, https://doi.org/10.1111/j.1365-246X.2006.02966.x, 2006.

698 Zheng, X.,F., Cheng, Z.,H., and Zhang, C. H.: The development of seismic monitoring
699 in Taiwan, Seismological and Geomagnetic Observation and Research, 26(3),
700 100-107, https://doi.org/10.3969/j.issn.1003-3246.2005.03.017, 2005 (in
701 Chinese).

702 Zhou, C., Zeng, X. Z., Wang, Q. L., and Liu, W. Y., and Wang, C. Z.: Rotational
703 motions of the Ms7.0 Jiuzhaigou earthquake with ground tilt data, Science China
704 Earth Science, 62(5), 832-842, https://doi.org/10.1007/s11430-018-9320-3, 2019.

705